Cracking property and brittleness evaluation of granite under high-temperature true triaxial compression in geothermal systems

Zaobao Liu, Chuan Wang, Mingshan Zhang, Jian-Fu Shao

Geomech. Geophys. Geo-energ. Geo-resour. (2023) 9:99
https://doi.org/10.1007/s40948-023-00631-2

RESEARCH

Cracking property and brittleness evaluation of granite under high-temperature true triaxial compression in geothermal systems

Zaobao Liu · Chuan Wang · Mingshan Zhang · Jian-fu Shao

Received: 26 April 2023 / Accepted: 17 June 2023

Abstract Cracking property and brittleness are critically important to the drillability of injection and production wells of enhanced geothermal systems. This paper is devoted to evaluating the cracking property and brittleness of the Gonghe granite under high-temperature true triaxial compression conditions through a series of laboratory tests. Thermal–mechanical coupled true triaxial compression tests were conducted on Gonghe granite samples under four representative temperatures (20 °C, 120 °C, 180 °C, and 240 °C) and three different minimum (5, 10, and 30 MPa) and intermediate (40, 60, and 75 MPa) principal stresses that correspond to the in-situ conditions of Gonghe geothermal reservoir. The strength, deformation, and cracking characteristics of the Gonghe granite are quantitatively evaluated from macro- to micro-scales based on the experimental results. Meanwhile, a novel brittleness index evaluation method considering both energy and failure surface roughness is proposed to accurately assess the brittleness strength of the Gonghe granite. We found that the strength of Gonghe granite is reduced by more than 20% when the temperature increases from room temperature to 240 °C. Higher temperature contributes to a smoother fracture surface and reduced brittleness of the Gonghe granite under thermal–mechanical coupled true triaxial compression. Our findings provide new insights for brittleness evaluation of the Gonghe granite formation and assist in efficient wells drilling design of enhanced geothermal systems.

Highlights

- We conduct thermo-mechanical coupled true triaxial compression tests on geothermal granite.
- Thermal degradation is quantified for the mechanical properties of Gonghe granite.
- Cracking features of Gonghe granite samples under varying load conditions are obtained.
- A new brittleness index evaluation method coupling elastic energy and JRC is proposed.

Keywords High-temperature granite · Thermal–mechanical coupled true triaxial compression · Fracture roughness · Brittleness index · Enhanced geothermal system

Z. Liu (✉) · C. Wang · M. Zhang · J. Shao
Key Lab of Ministry of Education on Safe Mining of Deep Metal Mines, College of Resources and Civil Engineering, Northeastern University, Shenyang 110819, Liaoning, China
e-mail: liuzaobao@mail.neu.edu.cn

J. Shao
CNRS, Centrale Lille, UMR 9013-LaMcube–Laboratoire de Mécanique, Multiphysique, Multi-échelle, Univ. Lille, 59000 Lille, France

Published online: 21 July 2023

1 Introduction

With ever-increasing worldwide energy demands, Enhanced Geothermal System (EGS) demonstrates broad application prospects as an economic and efficient energy source with huge reserves(Zhao et al. 2020; Olasolo et al. 2016; Lu 2018). Generally, the temperature of the EGS reservoir ranges from 150 to 650 °C corresponding to the buried depth of 3-10 km underground(Zhang et al. 2016; Wang et al. 2022). The hot dry granite is the most representative formation rock in the EGS projects exhibiting hard and brittle characteristics, which is closely related to its drillability of injection and production wells. Understanding the physical and mechanical properties of the brittleness granite under high-temperature and high-stress conditions plays an important role in maintaining the well stability and minimizing the drilling cost(Yan and Zheng 2017; Mahmutoglu 1998). Therefore, it is necessary and urgent to investigate the mechanical property and brittleness of the Gonghe granite under high-temperature and stress-coupled conditions.

Numerous laboratory experiments have been conducted to explore the thermal-physical and mechanical properties of rocks under thermo-mechanical coupled conditions. Many works have reported hard rock high-temperature mechanical experiments including uniaxial tests(Li et al. 2019; Rathnaweera et al. 2018; Wu et al. 2019), triaxial tests(Kumari et al. 2017; Masri et al. 2014; Xu and Karakus 2018; Zhang et al. 2018), and true triaxial compression tests(Zhao et al. 2019, 2018; Zhou et al. 2019; Miao et al. 2020; Liu et al. 2022; Gao et al. 2022). Additionally, the elastic-plastic behaviors of rocks, the deterioration mechanisms, and threshold points are carefully analyzed and quantified by high-temperature triaxial tests(Fang et al. 2016; Guo et al. 2018; Zhao et al. 2012; Zhang et al. 2015; Yang et al. 2021). It is well accepted that high-temperature has a significantly deteriorating effect on the physical and mechanical properties of rock, such as wave velocity, peak strength, peak strain, elastic modulus, and Poisson's ratio(Zhao et al. 2017; Siratovich et al. 2016; Liu and Xu 2015; Chen et al. 2012; Zhang et al. 2010; Zhou et al. 2022). For example, some thermal-mechanical triaxial compression tests have been conducted on granite samples from deep tunnel boreholes(Liu et al. 2022; Zhou et al. 2022) and some triaxial compression tests have been reported on granite samples at 400 °C under real-time high-temperatures although the temperature interval is large(Ma et al. 2020). However, there is a lack of detailed temperature research scope on the influence of real-time high-temperature, and the multiscale mechanical parameters and cracking modes of granite under different temperatures and true triaxial stress conditions remain unclear, while these properties are significant to the granite brittleness evaluation for borehole or geothermal deep well drillings.

The rock brittleness index is a key parameter commonly used in estimating the failure properties of rocks (Hucka and Das 1974; Altindag 2002; Munoz et al. 2016a; Zhang et al. 2016; Meng et al. 2021). A more violent failure process usually indicates a greater rock brittleness. Many mechanical responses related to rock failure processes, such as machinability and drillability of rock masses (Altindag 2002; Kahraman and Altindag 2004; Yagiz 2009; Yarali and Kahraman 2011; Olgay and Eren 2011; Özfırat et al. 2016; Nejati and Moosavi 2017; Gong et al. 2019; Zhang et al. 1367), are closely affected by rock brittleness. At present, brittleness is known as rock mechanical behavior and basic property (Hucka and Das 1974; Altindag 2002; Munoz et al. 2016a; Zhang et al. 2016; Meng et al. 2021). While different rock brittleness indicators are proposed (Hucka and Das 1974; Zhang et al. 2016; Meng et al. 2021, 2015; Martin 1996) since 1967, there is no conclusive definition to quantitatively describe it yet. Specifically, the rock brittleness indexes have been defined in various forms such as the strength ratio, the modulus ratio, and the energy index ratio (Zhang et al. 2016; Meng et al. 2021, 2015). Although the brittleness index has been widely used in different areas of rock engineering, the definition and measurement methods of rock brittleness haven't reached a consensus. Among them, the methods incorporating the energy coefficients are the most extensively used ones(Munoz et al. 2016a, 2016b; Zhang Xw et al. 1367; Meng et al. 2015; Kivi et al. 2018; Wang et al. 2020), which argued that both the deformation process and fracture behavior should be considered in the rock brittleness index.

For high-brittle rocks like the granite in EGS projects, it is difficult to directly obtain the post-peak stress-strain curves, which requires an alternative way to consider the post-peak behaviors of high-brittle rocks. When studying the post-peak behaviors, the cracking mode plays an important role in quantifying

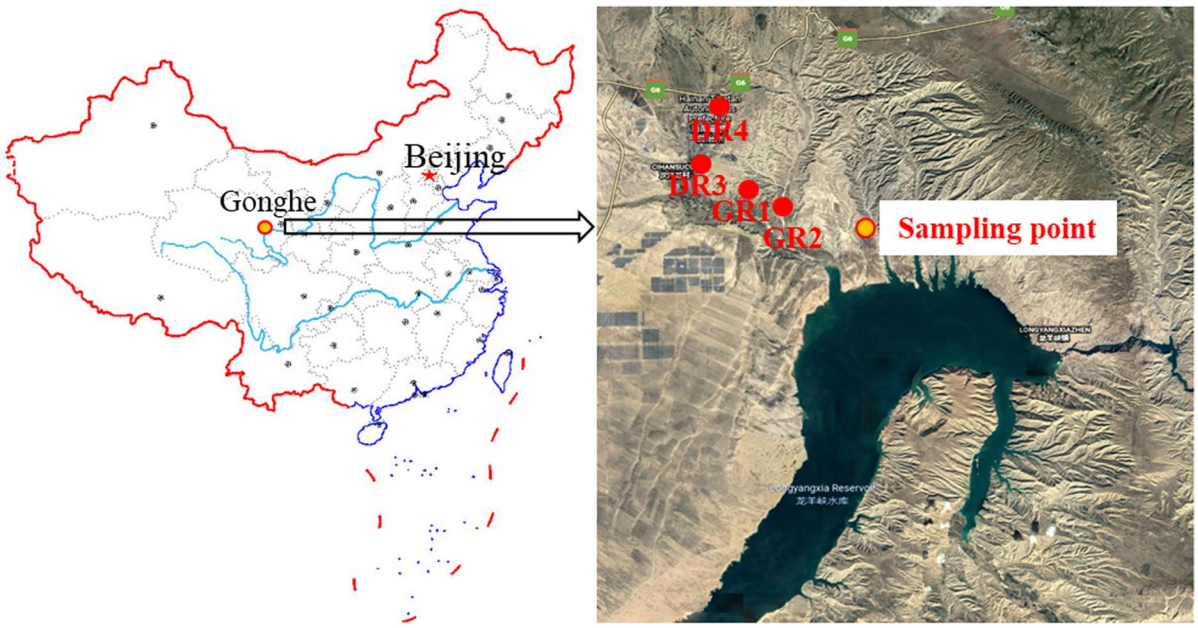

Fig. 1 General view of the origin of tested Gonghe granite samples

the brittleness of hard rocks. Since the joint roughness coefficient (*JRC*) has been used widely to describe the roughness of rock fracture surfaces(Belem et al. 2000; Fardin 2008; Huang et al. 2016; Zhang et al. 2017), it could be incorporated into the description of rock brittleness. However, it remains a major challenge to propose a robust brittleness index evaluation method incorporating the temperature effect and the post-peak behaviors to estimate the drillability of the high-brittle granite in EGS projects.

In the present work, we introduces the experimental results of thermal-physical properties and mechanical properties under high-temperature true triaxial compression of Gonghe granite through the self-developed real-time high-temperature true triaxial test system and develops a novel brittleness index evaluation method incorporating the energy index and *JRC* values to quantitatively estimate the high-brittle granite failure behaviors. The reminder of this work is organized as follows: Section 2 introduces the material thermal-physical properties of the Gonghe granite and the true triaxial compression test device as well as programs. The obtained strength, deformation, and cracking properties are given in Sect. 3. The brittleness indexes combined energy coefficients and *JRC* values are established to evaluate the brittleness index of rocks in Sect. 4. Finally, conclusions are presented in Sect. 5.

2 Material and method

2.1 Material and sample preparation

The granite samples tested in this study were obtained from the Gonghe area, Qinghai Province, China (see Fig. 1). The Gonghe Basin is located in Hainan Tibetan County with the main geothermal reservoir distributed in the Qiabuqia town. The total theoretical hot-dry-rock resource in the Qiabuqia geothermal reservoir is estimated to be about 1.638×10^{21} J, equivalent to 5.591×10^{10} t of standard coal(Lei et al. 2019). Since the 1960s, a series of hot-dry-rock and geothermal water exploration boreholes has been built up, four of which with temperatures over 180 °C. In 2017, the highest temperature of 236 °C at a depth of 3705 m was reported in the GR1 borehole.

The basic mechanical parameters of the tested representative samples of the Gonghe granite are shown in Table 1. The average density and P-wave velocity of the samples was 2.79 g/cm^3 and 5768 m/s, respectively. In the sample preparation process, the

Table 1 Basic parameters of the tested representative Gonghe granite samples

Sample No.	$L*B*H$ (mm^3)	Density (g/cm^3)	Wave velocity (m/s)	T (℃)	σ_2 (MPa)	σ_3 (MPa)	σ_p (MPa)	E (GPa)	Fracture angle θ (°)
GH14	50.00*50.12*99.81	2.595	5941	*RT*	40	30	583.08	62.73	80.0
GH13	50.17*50.18*100.07	2.593	5686	120	40	30	573.19	62.30	80.5
GH03	50.13*50.05*100.05	2.596	5783	180	40	30	551.42	59.39	80.2
GH04	49.83*50.04*100.02	2.594	5748	240	40	30	460.09	59.78	80.7
GH05	50.17*50.24*100.17	2.594	5757	180	40	5	355.86	57.74	84.2
GH06	50.1*49.94*99.98	2.597	5740	180	40	10	404.81	58.86	83.3
GH11	50.01*49.97*99.81	2.596	5730	180	60	30	581.25	60.01	78.8
GH12	49.85*50.12*100.18	2.594	5757	180	75	30	637.88	61.86	77.6

method recommended by ISRM(Feng et al. 2019) was used to cut the rock block into 52 ×52 ×102 mm^3 cube rocks. Then the cuboid rock was ground into a smooth standard rock sample of 50 ×50 ×100 mm^3. The X-ray diffraction (XRD) test results of Gonghe granite samples are shown in Fig. 2. It is found that the dominant minerals consist of feldspar, quartz, and biotite with a total content of over 90%.

2.2 Thermophysical parameters of Gonghe granite

The thermophysical parameters of the rock sample including the thermal conductivity, thermal expansion coefficient, and specific heat capacity are measured before thermal-mechanical coupled tests. The testing device and rock sample processing are shown in Fig. 3.

The disk samples in Fig. 3a with a diameter of 50 mm and height of 25 mm were used for thermal conductivity measurement using the DRPL-3B thermal conductivity tester shown in Fig. 3d. The average measured thermal conductivity is 3.23 W/(m·K). For the thermal expansion tests, we adopted the cylindrical rock sample with a diameter of 8 mm and length of 50 mm as shown in Fig. 3b. The average linear expansion coefficient of 11.48×10^{-6}/K is obtained by the ZRPY-1000 thermal dilatometer tester as shown in Fig. 3e. The specific heat capacity was measured by the mixed cooling method. To ensure the accuracy of the test data, the small rock blocks in different parts were ground into powder as shown in Fig. 3c with a diameter of less than 1 mm to meet the test requirements. The BRR-type specific heat capacity tester for rocks in Fig. 3f is used to measure the specific heat capacity coefficient. The average specific heat

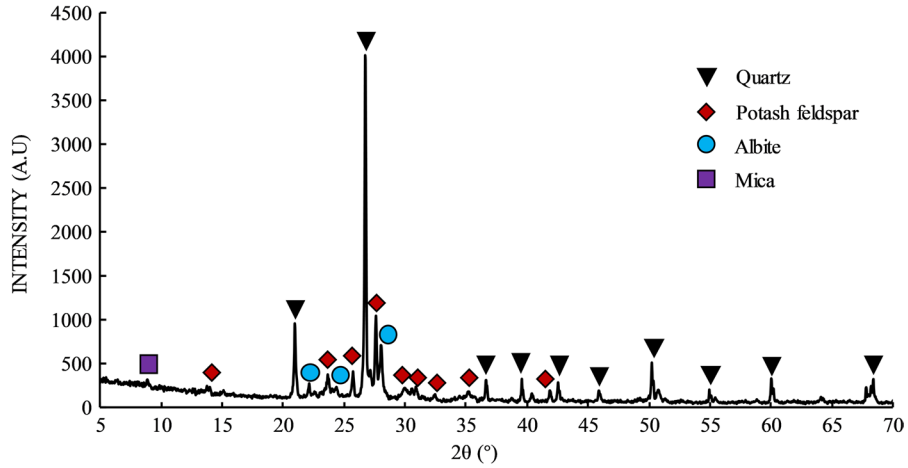

Fig. 2 XRD spectrum of the Gonghe granite powder

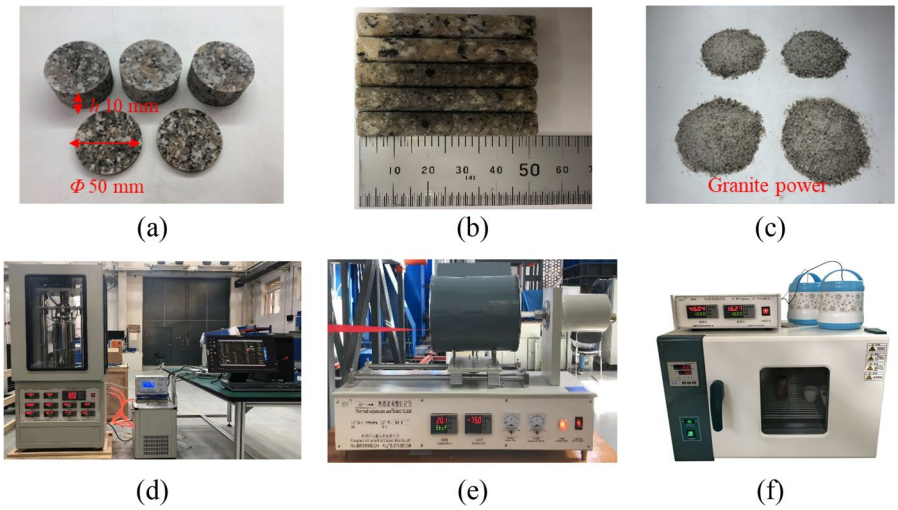

Fig. 3 Test equipment and sample preparation for thermal physical parameters of Gonghe granite. **a** Thermal conductivity test disc sample; **b** Thermal expansion coefficient test cylinder sample; **c** Specific heat capacity test powder samples. **d** Thermal conductivity tester; **e** Thermal expansion coefficient tester; **f** Specific heat capacity tester

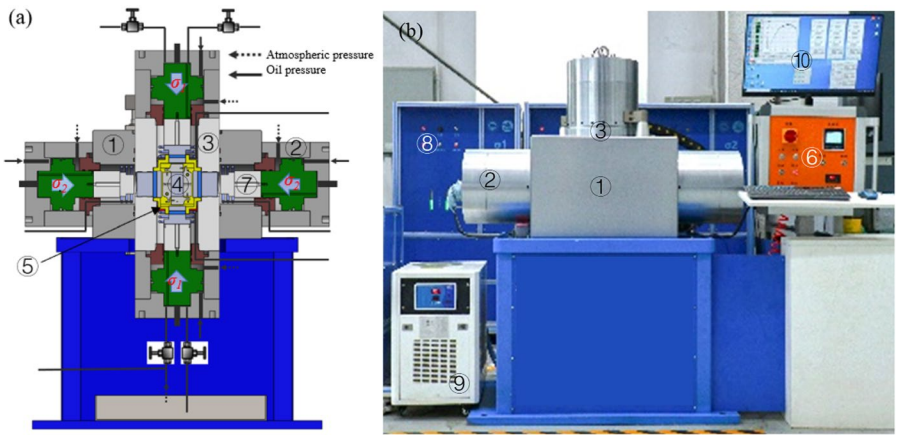

Fig. 4 Figure of true triaxial test system under high temperature and high pressure. **a** Schematic diagram, **b** Overview of the testing device. ① High temperature and high pressure test chamber; ② Loading cylinder; ③ Holder; ④ Specimen; ⑤ Incubator; ⑥ Temperature controller; ⑦ Load sensor; ⑧ Loading pump; ⑨ Cooling; ⑩ PC

capacity is obtained as 738.44 J /(kg·K). The thermophysical properties of Gonghe granite are consistent with previous works (Li et al. 2020, 2021). The above results prove that Gonghe granite has excellent heat storage capacity. The high thermal conductivity indicates that the heat-transfer medium in the EGS project can extract more energy from the reservoir for power generation.

2.3 Thermal–mechanical test system and procedure

The thermal-mechanical tests were carried out by the high-temperature and high-stress true triaxial hard rock test system(Wang et al. 2022) (see Fig.4). The real-time high-temperature loading module is mainly composed of an incubator, electric heating board, and temperature thermostat with stable real-time heating temperature scope ranging from 20 to 250 °C. The principal stress loading cylinder performs rigid stress loading in the σ_1 and σ_2 directions up to 2000 kN, while the σ_3 direction adopts flexible loading up to 70 MPa. The LVDTs are used to measure the deformation in the ε_1, ε_2, and ε_3 directions with measurement ranges of ±2.5 mm and accuracy of 1 μm. During the test, the principal stress σ_1 was controlled by the strain rate in σ_3 direction and the temperature is maintained by the temperature thermostat in the incubator. The specific testing conditions are summarized in Table 1.

The thermal–mechanical coupled tests were carried out in the following steps:

i. Increase the hydrostatic pressure (confining pressure) at a rate of 0.5 MPa/s to a prescripted value, 30 MPa for example ($\sigma_1=\sigma_2=\sigma_3$).
ii. Keep the pressure σ_3 constant, and start heating in the cell to reach the predetermined temperature value such as 120 ℃, 180 ℃, and 240 ℃, at the rate of 5 ℃/min by the thermostat.
iii. Stabilize the temperature and stress in the cell for 2 h, and increase the stress σ_1 and σ_2 simultaneously at a rate of 0.5 MPa/s to the predesigned value.
iv. Load the stress σ_1 at the constant ε_3 strain rate of 1×10^{-6} /s (0.003 mm/min) until the sample failure appears.

3 Experimental results

3.1 Stress–strain curves

The deviatoric stress-strain curves of Gonghe granite at different high-temperature and stress conditions are shown in Fig. 5. In the curves, *T* stands for temperature; σ_1, σ_2 and σ_3 respectively refer to the maximum principal stress, intermediate principal stress, and minimum principal stress; ε_1, ε_2, and ε_3 respectively denotes the maximum principal strain, intermediate principal strain, and minimum principal strain; ε_v represents the volumetric strains; the strains mean compression in positive directions and dilation in negative directions of the coordinate system. The axial strain-stress curve retraction is observed in the post-peak phase as depicted in Fig. 5a, c, and e, indicating the type II failure form of the Gonghe granite under the true triaxial compression. The elastic and crack propagation phases take place in the pre-peak deformation, and the initial compaction phase only accounts for a small proportion of the curves.

In the pre-peak phase, the strains in the three principal directions of the rock sample follow the order $\varepsilon_1>\varepsilon_2>\varepsilon_3$. While in the post-peak phase, ε_3 increases rapidly as ε_1 decreases. In the post-peak phase, the ε_1 strains decrease compared to the increase in the pre-peak phase, there is obvious fluctuation and partial automatic loading and unloading cycles in the post-peak stage. The ε_2 strains demonstrate a transition trend from compression to expansion due to the temperature change. Under high-stress conditions, the post-peak deformation appears as a minor expansion deformation; under high-temperature conditions, it behaves as a compression deformation. Therefore, high-temperature and stress effects work differently on the ε_2 strains of the Gonghe granite. In the post-peak phase, the σ_1 stress decreases rapidly in Fig. 5a, which indicates that the Gonghe granite exhibits an high-brittle characteristic during the true triaxial compression.

3.2 Peak stress

The peak stress variation with principal stress and temperature difference of the representative tested Gonghe granite samples are shown in Fig. 6 and the peak stress value is listed in Table 1 as well. It shows that the peak stress increases linearly with the growth of principal stress. The increase of intermediate principal stress (>40 MPa) leads to a slight increase in peak stress, while the peak stress change is more prominent for the minimum principal stress (<40 MPa) range. The peak stress increases by 15.68% from 551.42 MPa to 637.88 MPa when σ_2 increases from 40 to 75 MPa. Similarly, the peak stress increases by 54.95% from 355.86 to 551.42 MPa when σ_3 increases from 5 to 30 MPa.

Moreover, the peak stress of Gonghe granite is largely affected by temperature as shown in Fig. 6b, showing a negative correlation between the peak stresses and temperatures. The peak stress value is decreased by 21.09% when the temperature increases from 20 to 240 °C with a stress difference of 122.99 MPa. ΔT represents the temperature increment to *RT*, $\Delta T = T$-20, 20 °C $\leq T \leq$ 240 °C. To better illustrate the evolution trend of peak stress with temperature change, a linear function is proposed as follows:

$$\sigma_p = \alpha\,\Delta T + \beta \tag{1}$$

where α and β are the material parameters affected by rock type and temperature with units respectively of MPa/℃ and MPa. According to the fitted results, when $\sigma_2=40$ MPa and $\sigma_3=30$ MPa, one obtains $\alpha=-0.5085$, $\beta=602.61$.

3.3 Elastic modulus

The elastic modulus of Gonghe granite under different stress and temperature conditions is depicted in

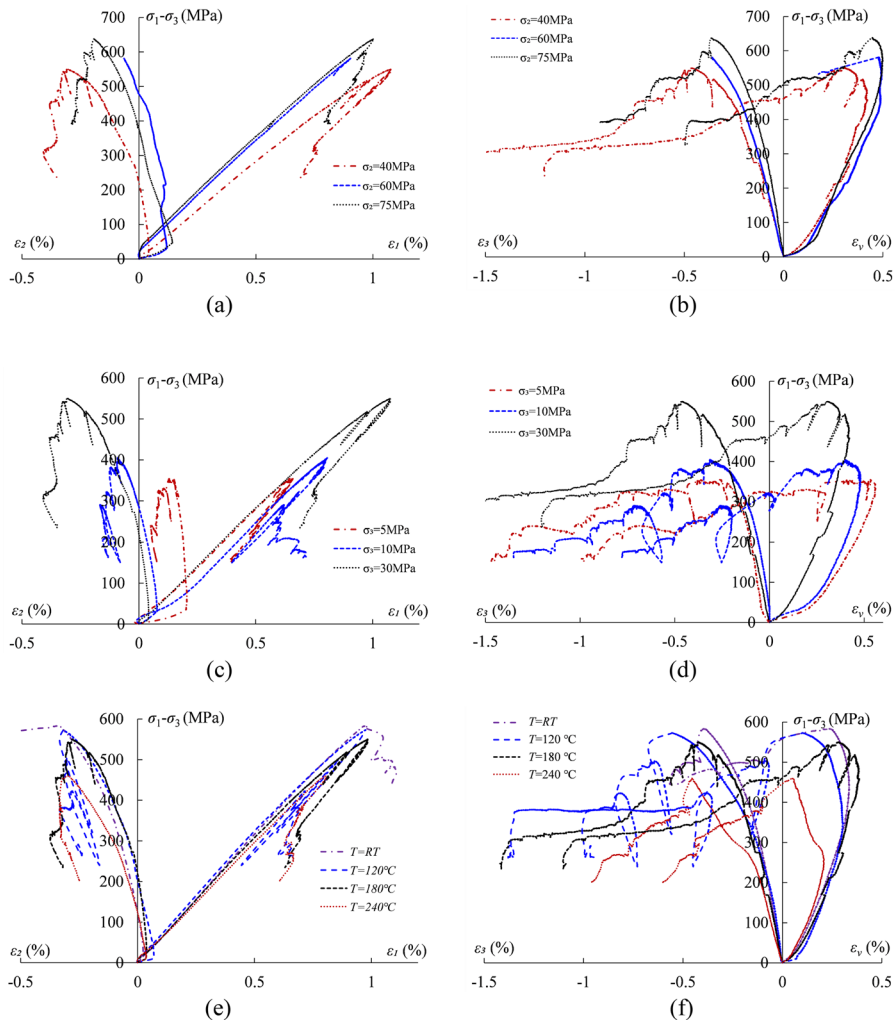

Fig. 5 Deviatoric stress–strain curves of Gonghe granite under high-temperature and pressure true triaxial compressions. **a** Deviatoric stress change with ε_1 and ε_2 at $T=180$ °C, $\sigma_3=30$ MPa with different intermediate principal stress; **b** Deviatoric stress change with ε_3 and ε_v at $T=180$ °C, $\sigma_3=30$ MPa with different intermediate principal stress; **c** Deviatoric stress change with ε_1 and ε_2 at $T=180$ °C, $\sigma_2=40$ MPa with different minor principal stress; **d** Deviatoric stress change with ε_3 and ε_v at $T=180$ °C, $\sigma_2=40$ MPa with different minor principal stress; **e** Deviatoric stress change with ε_1 and ε_2 of the tests under different temperatures at $\sigma_2=40$ MPa, $\sigma_3=30$ MPa; **f** Deviatoric stress change with ε_3 and ε_v of the tests under different temperatures at $\sigma_2=40$ MPa, $\sigma_3=30$ MPa

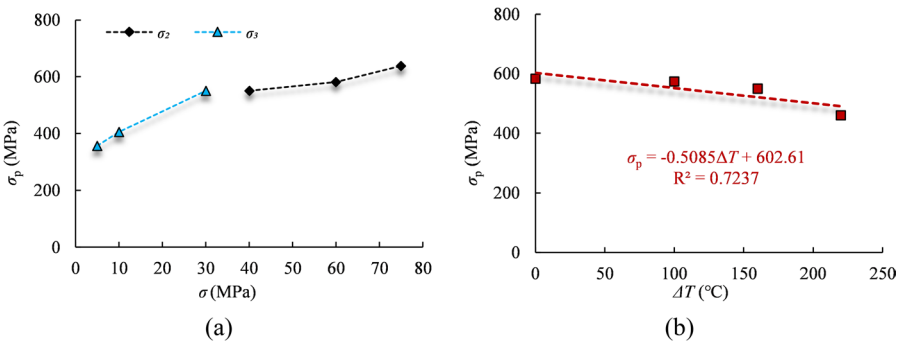

Fig. 6 Peak stress change of Gonghe granite with stress and temperature. **a** with stresses at $T=180$ °C; **b** with temperature increment at $\sigma_2=40$ MPa, $\sigma_3=30$ MPa

Fig. 7 and we also present their values in Table 1. The elastic modulus (E) is obtained based on the stress-strain curves in Fig. 5 by calculating the slope of the linear part. It shows that the elastic modulus is almost unchanged (<5%) when the surrounding environment changes. Therefore, we conclude that the elastic modulus is almost not affected by the stress and temperature conditions tested in this study.

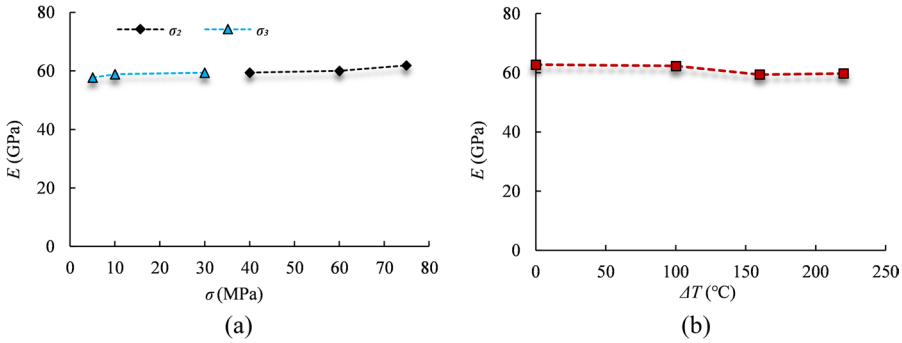

Fig. 7 Elastic modulus change of Gonghe granite with stress and temperature. **a** with stresses at $T = 180$ °C; **b** with temperature increment at $\sigma_2 = 40$ MPa, $\sigma_3 = 30$ MPa

3.4 Crack initiation stress and damage stress (σ_{ci} and σ_{cd})

The typical deviatoric stress-axial strain curve of the rock sample in the true triaxial compression test is shown in Fig. 8a. Five stages can be identified from the stress-strain curve : (I) crack compaction phase; (II) elastic phase; (III) crack stable growth phase; (IV) unstable crack propagation phase; (V) post-peak phase(Brotons et al. 2013).

Combined with the work of Gao(Gao et al. 2018), in the true triaxial compression test, the formula for calculating the sum of strains generated by cracks is given as follows:

$$\begin{aligned}\varepsilon_v^c &= \varepsilon_1^c + \varepsilon_2^c + \varepsilon_3^c = \varepsilon_1 + \varepsilon_2 + \varepsilon_3 \\ &\quad - ((1 - \mu_2 - \mu_3)(\sigma_d + \sigma_b))\ /E\end{aligned} \tag{2}$$

where ε_v^c is the volumetric strain generated by cracks, ε_1^c, ε_2^c and ε_3^c are the maximum, intermediate, and minimum principal crack-induced strains respectively; σ_b is the predetermined value of deviator stress in the σ_2 direction, and σ_d is the deviatoric stress loading process in the σ_1 direction (Assuming σ_d is within the range of elastic loading phase). The crack volume strain ε_v^c experienced an increase followed by a drop, the σ_{ci} is determined at the position where ε_v^c achieves the maximum. On the other hand, the crack damage stress σ_{cd} is defined as the point at which the total volumetric strain ε_v reverses. The σ_{ci} and σ_{cd} are determined as shown in Fig. 8b.

The σ_{ci} and σ_{cd} of Gonghe granite at different temperature conditions are shown in Fig. 9. The value of σ_{ci} and σ_{cd} gradually decreases as the temperature

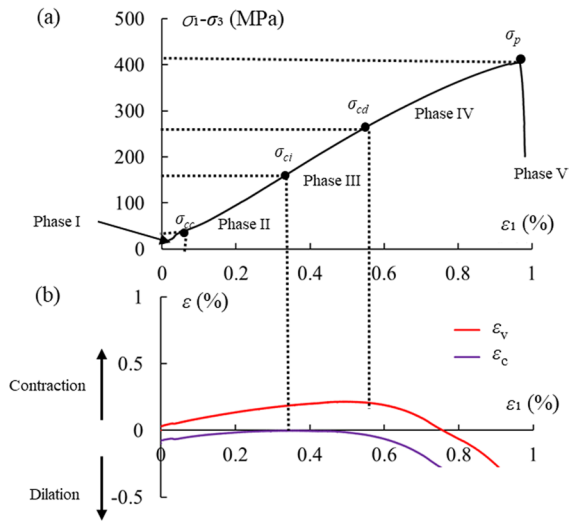

Fig. 8 Determination of crack initiation stress using the crack volumetric strain of the granite sample in true triaxial compression. **a** Stress–strain relationship, **b** the relationship between crack-induced strains and strain ε_1. σ_{cc} closure stress; σ_{ci} initiation stress; σ_{cd} damage stress; σ_p peak stress

increases from *RT* to 240 °C. Compared with the *RT,* the value of σ_{ci} and σ_{cd} is reduced by 50.18 MPa and 101.99 MPa respectively when the temperature reached 240 °C, corresponding to 24.17% and 39.37% of the *RT* conditions, indicating the significant weakening effect of temperature on σ_{ci} and σ_{cd}. In addition, the proportion of σ_{ci} is constantly increasing with the σ_{ci}/σ_{cd} ratio of 0.71, 0.72, 0.73, and 0.80, respectively when the temperature rises. In general, the peak stress variation trend with temperature is analogous to σ_{ci} and σ_{cd}.

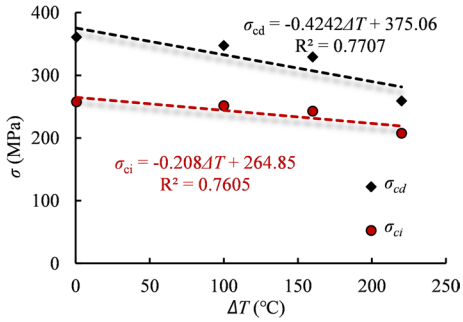

Fig. 9 The σ_{ci} and σ_{cd} of Gonghe granite at varying temperatures increment under $\sigma_2 = 40$ MPa, $\sigma_3 = 30$ MPa

3.5 Cracking properties

3.5.1 Fracture mode

The fracture characteristics of Gonghe granite samples under different stress and temperature conditions are shown in Fig. 10. One can see a localized major shear crack in each sample. The fracture of the rock sample is mainly parallel to the σ_2 direction and extends to a certain angle with σ_3 direction. Thus, the mode of rock fracture mainly appears as a compression-shear failure. Under different high-temperature conditions, the *V*-shaped fracture modes occur in the Gonghe granite, while the manifestations of secondary cracks are affected by the stress conditions. The increase of the intermediate principal stress results in a higher number of secondary cracks.

At the same time, two parallel secondary cracks can be observed at high intermediate principal stress (see Fig. 10f). The influence of the minimum principal stress on the failure mode is more obvious. With low minimum principal stress, the failure mode of Gonghe granite exists partial tensile failure characteristics (i.e., secondary cracks are parallel to the σ_1 direction). When the minimum principal stress is high, Gonghe granite presents a *V*-shaped failure mode, and the number of secondary cracks increases significantly. The failure mode of Gonghe granite changed from monoclinic to *V*-shaped failure as temperature increased.

The fracture angle defined as the angle between the longer part of the main crack's straight section and the bottom surface is shown in Fig. 11. It is found that the fracture angle decreases gently with the increase of intermediate principal stress and

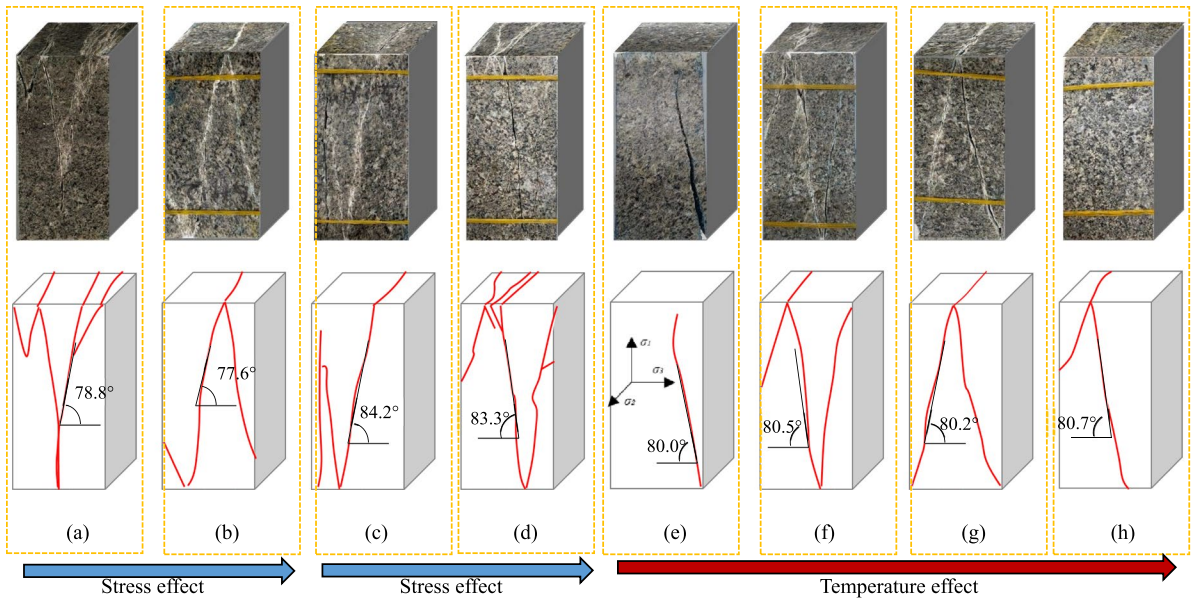

Fig. 10 Macroscopic fracture mode of Gonghe granite under thermo-mechanical coupling condition. **a** $T = 180$ °C, $\sigma_2 = 60$ MPa, $\sigma_3 = 30$ MPa; **b** $T = 180$ °C, $\sigma_2 = 75$ MPa, $\sigma_3 = 30$ MPa; **c** $T = 180$ °C, $\sigma_2 = 40$ MPa, $\sigma_3 = 5$ MPa; **d** $T = 180$ °C, $\sigma_2 = 40$ MPa, $\sigma_3 = 10$ MPa; **e** *RT*, $\sigma_2 = 40$ MPa, $\sigma_3 = 30$ MPa; **f** $T = 120$ °C, $\sigma_2 = 40$ MPa, $\sigma_3 = 30$ MPa; **g** $T = 180$ °C, $\sigma_2 = 40$ MPa, $\sigma_3 = 30$ MPa; **h** $T = 240$ °C, $\sigma_2 = 40$ MPa, $\sigma_3 = 30$ MPa

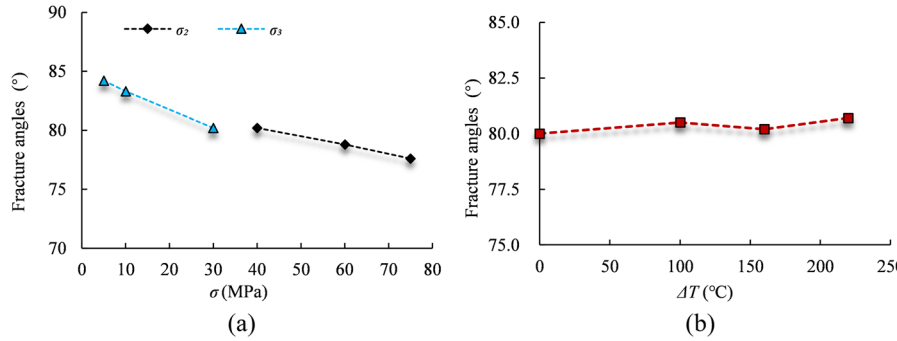

Fig. 11 Fracture angle change of Gonghe granite with stress and temperature. **a** with stresses at $T=180$ °C; **b** with temperature increment at $\sigma_2=40$ MPa, $\sigma_3=30$ MPa

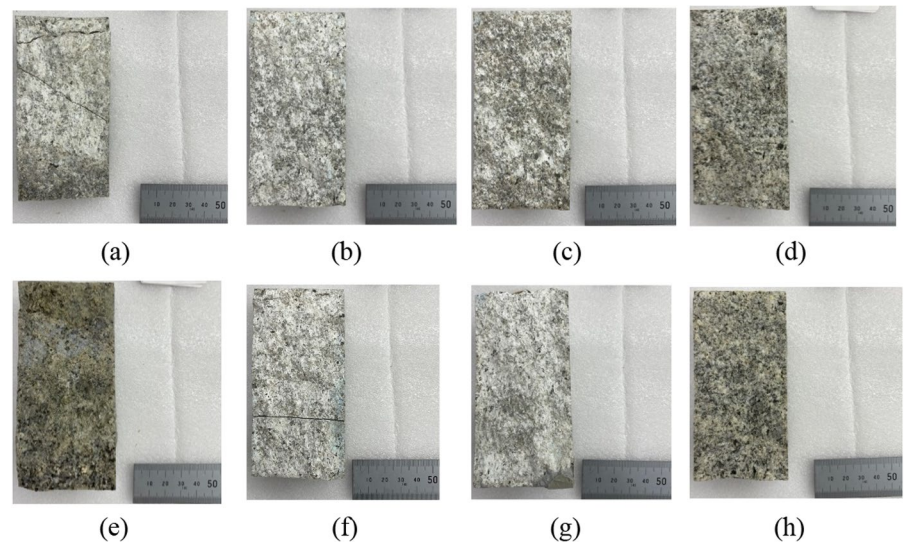

Fig. 12 Fracture surface of Gonghe granite sample under different stress and temperature. **a** $T=180$ °C, $\sigma_2=60$ MPa, $\sigma_3=30$ MPa; **b** $T=180$ °C, $\sigma_2=75$ MPa, $\sigma_3=30$ MPa; **c** $T=180$ °C, $\sigma_2=40$ MPa, $\sigma_3=5$ MPa; **d** $T=180$ °C, $\sigma_2=40$ MPa, $\sigma_3=10$ MPa; **e** *RT*, $\sigma_2=40$ MPa, $\sigma_3=30$ MPa; **f** $T=120$ °C, $\sigma_2=40$ MPa, $\sigma_3=30$ MPa; **g** $T=180$ °C, $\sigma_2=40$ MPa, $\sigma_3=30$ MPa; **h** $T=240$ °C, $\sigma_2=40$ MPa, $\sigma_3=30$ MPa

minimum principal stress in the range of 20-240 ℃, leading to an angle decrease of 2.6 ° and 4 °, respectively. It means the minimum principal stress shows a greater influence than the intermediate principal stress on the fracture angle. However, the effects of temperature on fracture angle are negligible with an angle change rate of less than 1%. Thus, in the EGS well drilling fieldwork, attention should be paid to the stress change other than the temperature for orientation control of the drilling well.

3.5.2 Macroscale

The images of the fracture surface for the Gonghe granite sample under different stress and temperature are shown in Fig. 12. The relatively intact structure of the damaged sample after failure is clearly observed from the figures. We also notice that the fracture surface is smooth with many rock powder particles on it. During the compression-shear mixing failure process, the generation of cracks promotes the continuous destruction of the integrity of the rock sample. Once the final failure occurs, several rock particles fall off under the shearing force.

The deformation and damaged appearance of the rock specimen section can give a preliminary understanding of the final form of the fracture specimen at the macroscopic level, while it is an intuitive impression of the fracture surface. To further explore fracture surfaces at the mesoscopic level, we select the complete fracture surface of the failed samples in the main crack to reconstruct their distribution pattern using the 3D laser scanning method. Meanwhile, the roughness of the fracture surface is carefully analyzed. The scanned figures of the fracture surface of the rock sample obtained by 3D laser scanning technology are shown in Fig.13.

During laser scanning, the slight deviation of the placement position of the fracture surface of the rock sample might lead to calculation errors in the absolute value height in the Z-direction. However, the difference in placement angle within a certain range does not affect the evaluation of roughness if the height difference between adjacent points is used for calculation. The joint roughness coefficient (*JRC*) is a key parameter to characterize surface roughness in geotechnical engineering. Tse and Cruden (1979)(Tse and Cruden 1979) proposed an empirical correlation statistical method based on 10 standard profiles of (Barton and Choubey 1977) as follows:

$$\boldsymbol{JRC} = 32.2 + 32.47\ \boldsymbol{log}(Z_2) \tag{3}$$

The Z_2 parameter is calculated in the discrete form as:

$$Z_2 = \sqrt{1/(N-1)\sum_{i=2}^{N}((z_i - z_{(i-1)})/(x_i - x_{(i-1)}))^2} \tag{4}$$

where x_i is one of N discrete points along the profile direction and z_i is the corresponding height values of the profile.

We adopt here the algorithm proposed by (Heinze et al. 2021) for the *JRC* calculations. During the analysis of *JRC*, about one hundred straight lines are taken at an interval of 0.5 mm in the X-direction to calculate the *JRC* in the Y-direction. The final *JRC* value of the sample is obtained by averaging all the straight-line *JRC* values in the Y-direction. The Y-direction *JRC* calculation result of the fracture surfaces of different rock samples is shown in Fig. 14.

Under different intermediate principal stress conditions, the *JRC* varies a lot while *JRC* shows a minor increasing trend with the increase of minimum principal stress. On the other hand, with the increase in temperature, *JRC* shows a rapid decrease trend. Nejati found that rock brittleness is associated with fracture surface roughness, low-brittleness rocks generate a smoother failure surface than high-brittleness rocks(Nejati and Ghazvinian 2014). Therefore, the decrease of the *JRC* of the Gonghe granite with temperature reflects a weaker brittleness. The relationship between *JRC* and temperature can be approximately quantified using an exponential function with the formula:

$$JRC = me^{n\Delta T} \tag{5}$$

where m and n are the constant parameters related to the material properties of the rock which can be obtained from the experimental results. In this work, we got the m and n values of 9.461 and - 0.005737, respectively, based on the *JRC* results with R^2 of 0.9851.

3.5.3 Mesoscale

To study the microscopic mechanism of the Gonghe granite after failure, this work uses a VHX-2000 ultra-depth-of-field 3D optical microscope to monitor the mesoscopic structure of the rock failure surface, and the results are shown in Fig. 15. Under different temperature conditions, the fracture surface of the rock sample has a step-like structure. With the increase in temperature, the height and number of steps that formed tend to decrease. The 4-layer structure at *RT* is reduced to 3-layer at 120 °C and 180 °C and further evolves to 2-layer when the temperature reaches 240 °C. The variation in the number of steps represents the change in the roughness of the fracture surface and decreased brittleness of granite, which is in line with the macroscale observations as discussed in the previous section.

3.5.4 Microscale

The scanning electron microscope (SEM) images of fracture morphology under different temperature conditions are plotted in Fig. 16 to carefully check the surface microstructure (x500) of the Gonghe granite samples. The river-line and step cleavage are well developed in the fracture patterns of rock particles. With the increase in temperature, the number of both fluvial and stepped cleavages declines rapidly while the surface is always dominated by stepped cleavages.

In the process of rock brittle failure, the grains suffered from different degrees of damage, which is evidenced by intergranular and transgranular failures

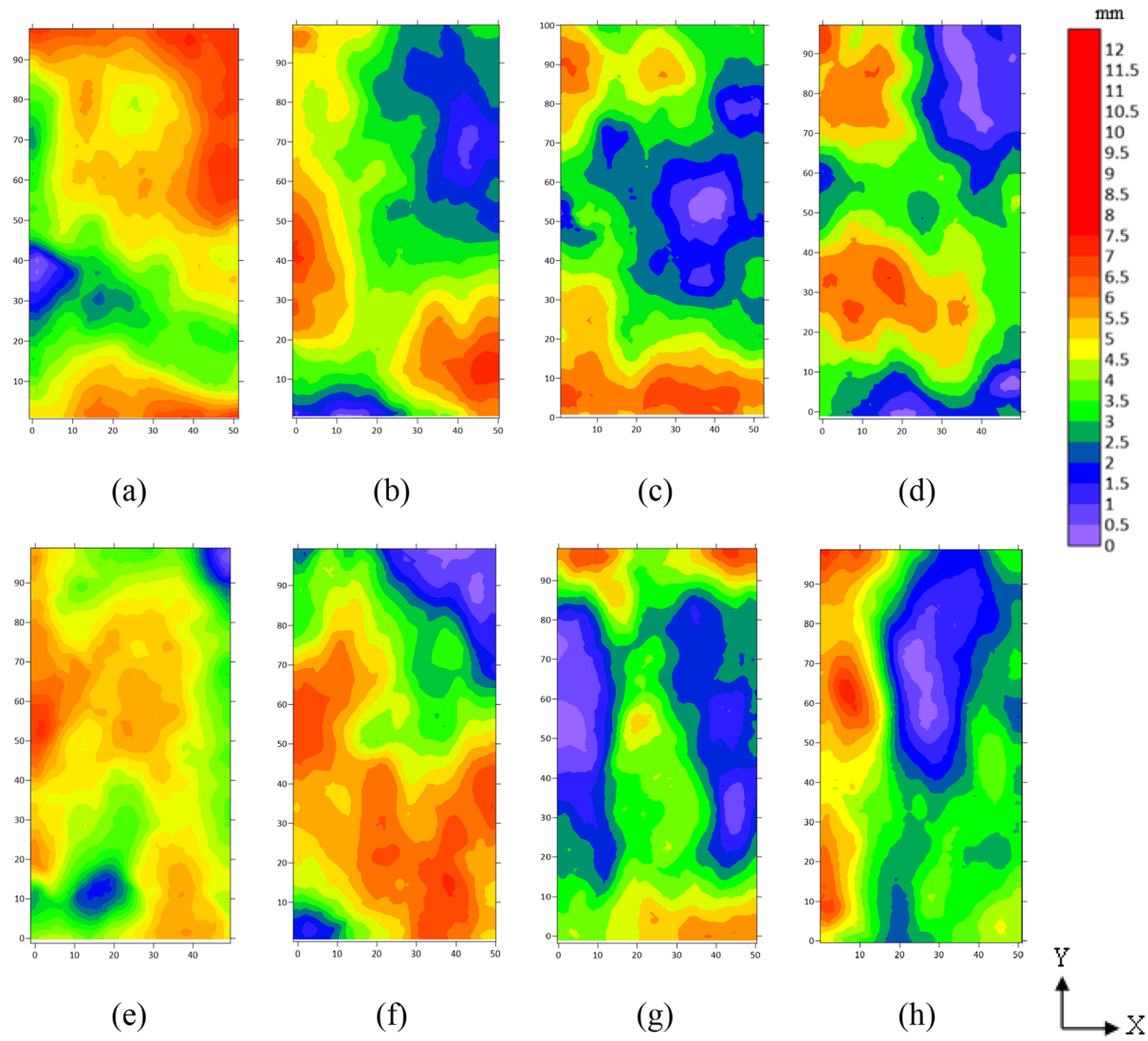

Fig. 13 3D laser scanning images of the fracture surface of Gonghe granite under different stress and temperature. **a** $T=180$ °C, $\sigma_2=60$ MPa, $\sigma_3=30$ MPa; **b** $T=180$ °C, $\sigma_2=75$ MPa, $\sigma_3=30$ MPa; **c** $T=180$ °C, $\sigma_2=40$ MPa, $\sigma_3=5$ MPa; **d** $T=180$ °C, $\sigma_2=40$ MPa, $\sigma_3=10$ MPa; **e** *RT*, $\sigma_2=40$ MPa, $\sigma_3=30$ MPa; **f** $T=120$ °C, $\sigma_2=40$ MPa, $\sigma_3=30$ MPa; **g** $T=180$ °C, $\sigma_2=40$ MPa, $\sigma_3=30$ MPa; **h** $T=240$ °C, $\sigma_2=40$ MPa, $\sigma_3=30$ MPa

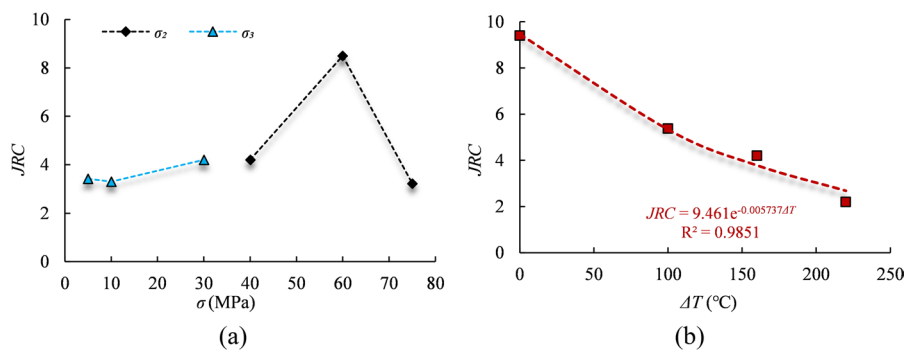

Fig. 14 *JRC* change of Gonghe granite with stress and temperature. **a** with stresses at $T=180$ °C; **b** with temperature increment at $\sigma_2=40$ MPa, $\sigma_3=30$ MPa

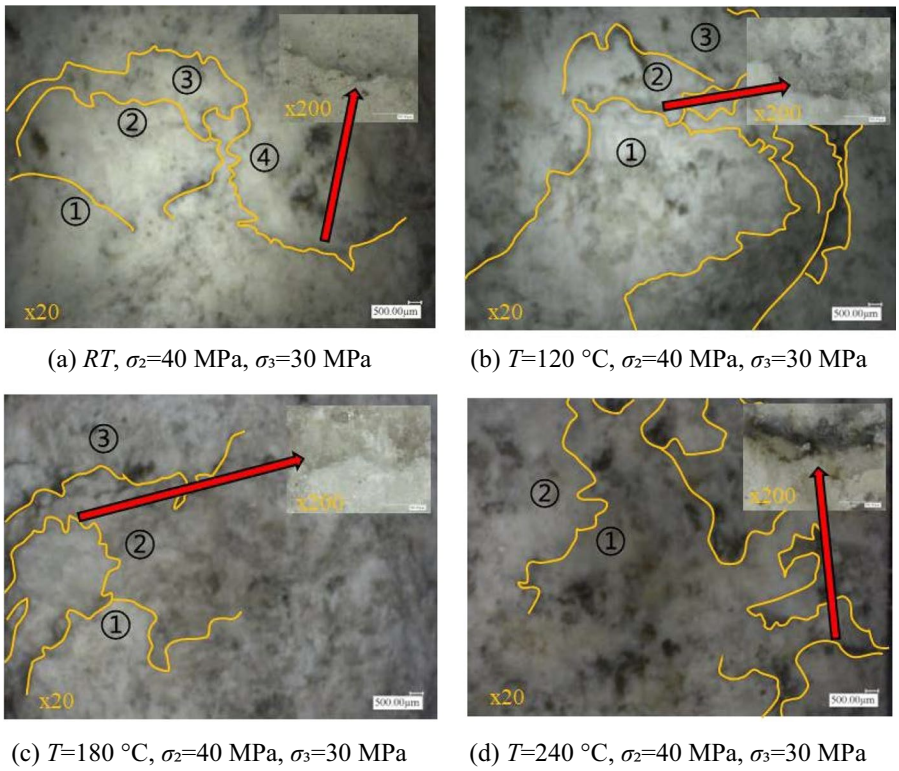

(a) *RT*, σ_2=40 MPa, σ_3=30 MPa (b) *T*=120 °C, σ_2=40 MPa, σ_3=30 MPa

(c) *T*=180 °C, σ_2=40 MPa, σ_3=30 MPa (d) *T*=240 °C, σ_2=40 MPa, σ_3=30 MPa

Fig. 15 Optically magnified images of the fracture surface of Gonghe granite at different temperatures

in Fig. 16c. Brittleness transgranular fracture plays the dominant role in the failure of the specimen and the fracture mechanisms include shear and cleavage fracture. At the same time, the original micropores as observed in Fig. 16b provide favorable conditions for the formation of intergranular fractures. During the process of crack propagation along the grain boundary, the grains at the boundary are squeezed and fractured, making transgranular fracture one of the brittleness fracture forms. Moreover, the grain joint structure of the rock is reduced at a higher temperature condition, leading to a smooth fracture surface.

According to the comprehensive analysis of the fracture characteristics at different scales, it is believed that the increase in temperature promotes thermal stress to generate more microcracks, providing a more direct optimal path for crack propagation during stress loading, thus generating a smooth main crack. Consequently, we conclude that the increasing temperature significantly reduces the roughness of the fracture surface.

4 Discussion

4.1 Mechanical property degradation under high stress and temperature

It is well known that high-temperature would weaken the mechanical properties of rock to some extent either after heat treatment or in real-time high-temperature conditions(Wang et al. 2015; Shang et al. 2019; Wong et al. 2020). Due to the complicated geothermal conditions, the impact of high temperatures on rock mechanics might vary from each other. In this study, we discussed the influence of temperature on the peak stress and elastic modulus of rock and compared the real-time high-temperature testing experimental results with previously published work of Ma(2020), Guo(2018), Yin(2021), and Feng(2018). Considering the difference in test conditions, the normalized method is proposed and the results are shown in Fig. 17.

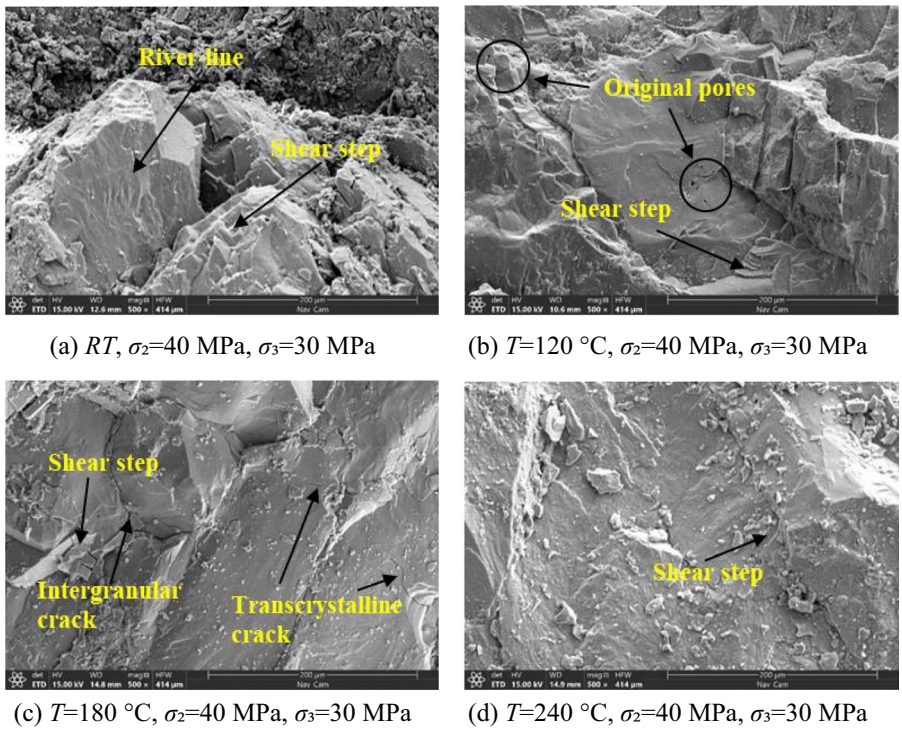

(a) *RT*, σ_2=40 MPa, σ_3=30 MPa (b) *T*=120 °C, σ_2=40 MPa, σ_3=30 MPa

(c) *T*=180 °C, σ_2=40 MPa, σ_3=30 MPa (d) *T*=240 °C, σ_2=40 MPa, σ_3=30 MPa

Fig. 16 SEM images of the fracture surface of Gonghe granite at different temperatures

In Fig. 17, we observed that the peak stress and elastic modulus are heavily affected by temperature under different stress levels and exhibit different changing trends. The influence of thermo-mechanical coupling on the elastic modulus is more complicated. Ma et al. reported that the peak stress increases with increasing temperature while the peak stress-increasing process is adversely suppressed at high temperature and stress conditions. By contrast, Yin et al. argued that the modulus of granite decreases or fluctuates with the increase in temperature. Guo et al. also noticed a significant decrease in the peak stress with increasing temperature. The increase of the stress level would significantly promote the reduction of the peak stress and both temperature and the stress contribute to the damage aggravation. The temperature comes into effect when the temperature ranges from 300 to 350 °C. While our study reveals a similar trend as Guo's study, that is, the temperature significantly weakens the strength and elasticity, the effect degree is different. One main reason could be attributed to the difference in stress loading conditions.

To further investigate the effect of temperature on the mechanical parameters of granite, we performed a normalized analysis of the mechanical parameters of granite. Fig. 18 shows the normalized results of the mechanical parameters of Gonghe granite under different temperature conditions. σ_p, σ_{ci}, and σ_{cd} decrease slowly followed by a sharp drop when the temperature is higher than 180 °C, which is considered to be the critical temperature on the influence of the mechanical parameters of Gonghe granite. We also noticed that the effects of temperature on σ_p and σ_{ci} are the same, whereas it results in a lower σ_{cd} at the same condition.

4.2 Brittleness index of ultra-brittle granite at high temperature

4.2.1 Stress threshold method (σ_{ci} and σ_{cd})

The strength parameters σ_c and σ_t (uniaxial compressive strength and Brazilian tensile strength) were first used to calculate the brittleness index B_1, which is expressed as:

$$B_1 = \sigma_c / \sigma_t \tag{6}$$

The calculation formula of the brittleness index was extended subsequently based on Eq.6 by taking

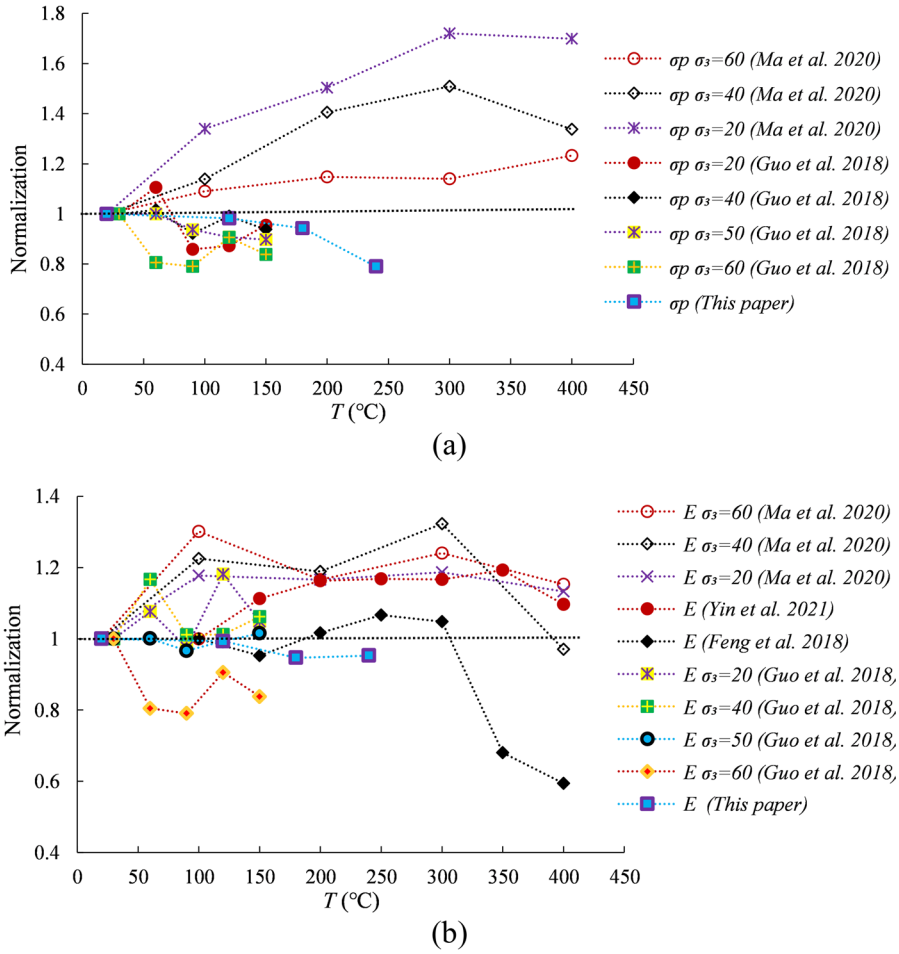

Fig. 17 Normalized comparison of mechanical parameters affected by temperature in different granite tests. **a** Strength normalization; **b** Elastic modulus normalization

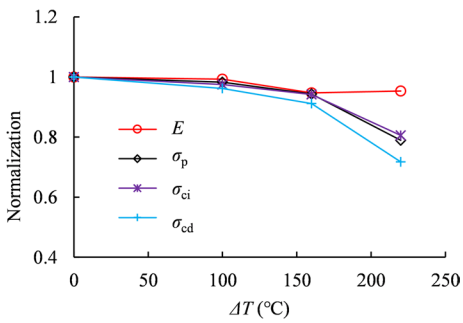

Fig. 18 Normalization of mechanical parameters of Gonghe granite at different temperatures

σ_{ci} into account, using σ_{ci} and σ_t to calculate the brittleness index, which is defined as:

$$B_2 = \sigma_{ci} / \sigma_t \tag{7}$$

Inspired by the results of the high-temperature and high true triaxial stress test conditions given above, we improved Eq. (7), and the true triaxial compressive strength (σ_p) was applied. Here, σ_{cd} is used to characterize the brittleness index, expressed as:

$$B_3 = \sigma_{ci} / \sigma_p \tag{8}$$

$$B_4 = \sigma_{cd} / \sigma_p \tag{9}$$

The σ_{ci} and σ_{cd} obtained by the appeal calculation are substituted into Eq. (8) and Eq. (9), respectively to calculate B_3 and B_4, and the results are shown in Fig. 19. Recalling the analysis in Sect. 4, the difference in the fracture modes represents a significant change in brittleness, and the brittleness decreases significantly with the increase in temperature. As a result, the narrow variation range of B_4 is unable to

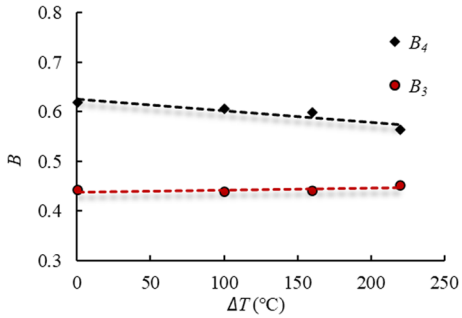

Fig. 19 Variation of brittleness index calculated by threshold stress method with temperature increment under $\sigma_2 = 40$ MPa, $\sigma_3 = 30$ MPa

reflect the dramatic change characteristics of rock brittleness.

At the same time, B_3 exhibits an increasing trend with increasing temperature, which is exactly the opposite of the analysis in Sect. 4. It might be because the value of σ_{ci} is largely affected by artificial factors. In general, B_3 and B_4 are not applicable to accurately express the brittleness index of ultra-brittleness rocks.

4.2.2 *Energy and JRC combined method*

As indicated in Sect. 3, the Gonghe granite shows an high-brittle behavior during the true triaxial compression under high-temperature and stress-coupled conditions corresponding to the EGS working situations. The brittleness from the stress threshold method can only consider the pre-peak behavior of rocks. It is necessary to propose a novel brittleness index that considers both pre-peak and post-peak behaviors. The pre-peak behaviors of rocks can be well described by stress or energy accumulated during loading but the post-peak ones cannot. As known, energy releases do exist in the rock post-peak phase(Munoz et al. 2016a) and the *JRC* has close correlations to the brittle failure of rocks(Yong et al. 2018). Hence, we propose the novel brittleness index based on pre-peak energy and post-peak fracture *JRC*.

The pre-peak energy calculation is shown in Fig. 20, and the brittleness index is calculated:

$$U_e = 1/2(\varepsilon_f - \varepsilon_p)\sigma_p \tag{10}$$

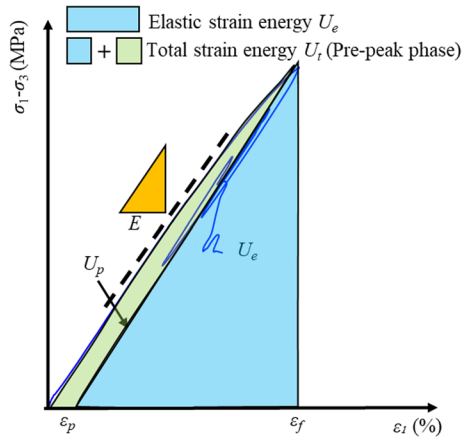

Fig. 20 Energy evolution of brittleness rocks in a typical stress–strain curve (ε_p is plastic strain; ε_f is the strain at peak state; U_e is elastic strain energy; U_p is the plastic strain energy and E is elastic modulus)

$$U_t = U_e + U_p = \int_0^{\varepsilon_f} \varepsilon d\sigma \tag{11}$$

$$BI = \frac{U_e}{U_t}\sqrt{\frac{JRC}{B}} \tag{12}$$

where ε_p is the plastic strain, ε_f is the peak strain, U_e is the elastic energy, U_t is the total strain energy of the pre-peak phase, and B is the *JRC* value at the *RT* condition. The energy contribution of ε_2 and ε_3 ($\sigma_2 =$ 40 MPa and $\sigma_3 = 30$ MPa) is considered in the energy calculation process. The calculation method of elastic energy and pre-peak total energy is the same as σ_1.

It can be seen from Table 2 that the elastic energy, total energy, and the ratio of the elastic energy and total energy decrease with the increase in temperature. The results indicate that the calculated brittleness of the pre-peak energy is consistent with the results discussed in Sect. 4. It was pointed out that stronger brittleness of the rock required greater elastic strain energy and less additional input energy(Hucka and Das 1974). The elastic energy accounts for about 90% of the total energy based on our results, demonstrating the high-brittleness character of the Gonghe granite.

Table 2 Pre-peak strain energy for the Gonghe granite under different temperatures

Sample No.	ΔT (°C)	*Ue* (10^{-2} MJ/m^3)	*Ut* (10^{-2} MJ/m^3)	*Ue/Ut*	*JRC*
GH14	0	251.2373	268.8494	0.934491	9.43
GH13	100	240.4799	270.4607	0.889149	5.38
GH03	180	233.2464	266.812	0.874198	4.24
GH04	220	150.0495	174.932	0.857759	2.21

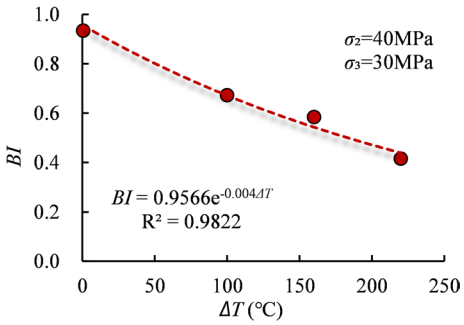

Fig. 21 Relationship between *BI* index and temperature increment of Gonghe granite

The calculation result of *BI* according to Eq. (12) is shown in Fig. 21. It is observed that *BI* decreases with the increase of temperature increment. When *JRC* is included in *BI*, an obvious brittleness decrease trend is obtained, which agrees well with the analysis in Sect. 3. A major challenge of high-brittleness rocks is to obtain key information from the stress-strain curve (type II) in the post-peak stage. The method proposed in this work provides a smart way to deal with this issue without any artificial factor interference in the calculation process.

We tested the Tibet granite to verify further the accuracy of the method of calculating *BI*. For simplification, we validate only the Tibet granite triaxial compression tests at 60 MPa confining pressure of different temperatures and keep the master lines of stress–strain curves. The energy index values of the pre-peak stage under different temperature conditions of the Tibet granite are shown in Table 3. One can find the energy index changes of two granites vary under different temperatures and stress conditions as indicated in Tables 2 and 3. The ratio of elastic energy in the pre-peak stage of Tibet granite is between 0.65 and 0.8, which is lower than that in the high-brittle Gonghe granite. The ratio of elastic energy increases with the increase in temperature. The *JRC* value of rock fracture surface also tends to increase with temperature.

The difference in brittleness of the granite is mainly due to their mineral compositions and loading conditions. The Gonghe granite contains less biotite and more quartz than the Tibet granite according to the rock particle composition (XRD) analysis. On the other hand, the confining pressure of the Gonghe granite sample is lower than that of the Tibet granite, and the loaded temperature level is higher than the latter. In addition, the intermediate principal stress may also affect the brittleness of the rock. A positive correlation shown in Fig. 22 is obtained between the *BI* of the Tibet granite sample and the temperature using Eq. (12). The *BI* of Tibet granite also tends to increase with temperature which agrees well with the calculated results, indicating the good reliability and robustness of the proposed brittleness calculation method.

In our work, the rock strength and deformation parameters are included to determine the brittleness index of rocks, while the brittleness characteristics of rocks can also be evaluated based on rock stress–strain curves, in which the brittleness index of rock mass is calculated by the post-peak stress drop rate and energy ratio. And calculate the brittleness

Table 3 Pre-peak strain energy and *JRC* of Tibet granite at *Pc* = 60 MPa under different temperatures

Sample no	*T* (℃)	*Ue* (10^{-2} MJ/m^3)	*Ut* (10^{-2} MJ/m^3)	*Ue/Ut*	*JRC*
C60RT	RT	289.154	422.545	0.684	11.97
C60T60	60	168.907	286.299	0.590	9.46
C60T90	90	204.762	311.394	0.658	14.94
C60T120	120	192.560	241.467	0.797	15.13

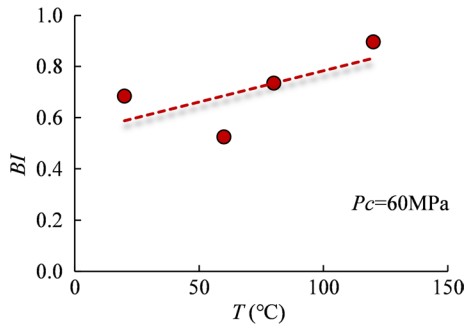

Fig. 22 Relationship between *BI* index and temperature of Tibet granite at *Pc* = 60 MPa

index of rock mass based on methods such as mineral composition determination, hardness test, impact test, nano-indentation test, and penetration test. Among them, the energy calculation method based on the stress–strain curve depends on the residual stress and strain parameters after the peak. However, it is difficult to accurately obtain the post-peak properties of highly brittle rocks, including residual features. Therefore, the brittleness index calculation method based on the post-peak curve properties is obviously not suitable for highly brittle rocks. This paper summarized the pre-existed representative brittleness calculation methods in Table 4 and computed the corresponding brittleness index in combination with the experimental results. The applicability and performance of each method is carefully discussed and compared with our model. According to the partial brittleness index calculation method listed in Table 4, combined with the high-temperature true triaxial test results of Gonghe granite, the brittleness index results (B_{11}-B_{31}) using various equations under different temperature conditions are shown in Table 5.

Table 4 Summary of the brittleness index calculation methods (Hucka and Das 1974; Protodyakonov 1962; Bishop 1967; Kidybiński 1981; Aubertin et al. 1994; Sun et al. 2013; Luan et al. 2014; Tarokh et al. 2016; Kuang et al. 2021; Liu et al. 2018; Gao et al. 2022)

Calculation method	Brittleness index calculation equation	References	Remark
Strength parameter	$B_{11} = 8\sigma_p/\sigma_{ci}$	Wang et al. (2014)	σ_p: Peak stress σ_{ci}: Cracking initiation stress σ_{cd}: Damage stress
	$B_{12} = \sigma_p\sigma_{ci}/16$		
	$B_{13} = \sqrt{\sigma_p\sigma_{ci}/16}$		
	$B_{14} = \sigma_{ci}/\sigma_p$	Tarokh et al. (2016) Gao et al. (2022)	
	$B_4 = \sigma_{cd}/\sigma_p$	This work	
Stress–strain curve	$B_{21} = \varepsilon_e/\varepsilon_p$	Hucka and Das (1974)	ε_e: Elastic strain ε_p: Peak strain ε_{ci}: Cracking initiation strain U_e: Elastic energy U_t: Total energy *B: JRC* at *RT*
	$B_{22} = (\varepsilon_p - \varepsilon_e)/\varepsilon_p$	Martin and Chandler (1996)	
	$B_{23}=U_e/U_t$ $B_{24}=U_t/U_e$	Hucka and Das (1974), Kidybinski (1981), Aubertin et al. (1994)	
	$B_{25}=[(\sigma_p - \sigma_{ci})/\sigma_p]/[(\varepsilon_p - \varepsilon_{ci})/\varepsilon_p]$	Liu et al. 2021	
	$B_{26}=(\sigma_p - \sigma_{ci})/[\varepsilon_p(\varepsilon_p - \varepsilon_{ci})]$	Kuang et al. 2021	
	$BI = \frac{U_e}{U_t}\sqrt{\frac{JRC}{B}}$	This work	
	$B_{31} = E/\nu$	Sun et al. 2013; Luan et al. 2014	

Table 5 Brittleness index calculation results

T (℃)	B_{11}	B_{12}	B_{13}	B_{14}	B_{15}	B_{21}	B_{22}	B_{23}	B_{24}	B_{225}	B_{26}	B_{31}	*BI*
20	18.09	9395.31	96.93	0.4421	0.6192	0.9549	0.0451	0.9345	1.0701	0.9584	589.35	154.48	0.9345
120	18.24	9002.30	94.88	0.4385	0.6060	0.9433	0.0567	0.8891	1.1247	0.9242	556.99	109.55	0.6727
180	18.14	8351.07	91.38	0.4414	0.5985	0.9425	0.0575	0.8742	1.1439	0.9260	525.93	138.46	0.5843
240	17.73	5970.55	77.27	0.4513	0.5630	0.9564	0.0436	0.8578	1.1658	0.9715	690.55	105.62	0.4150

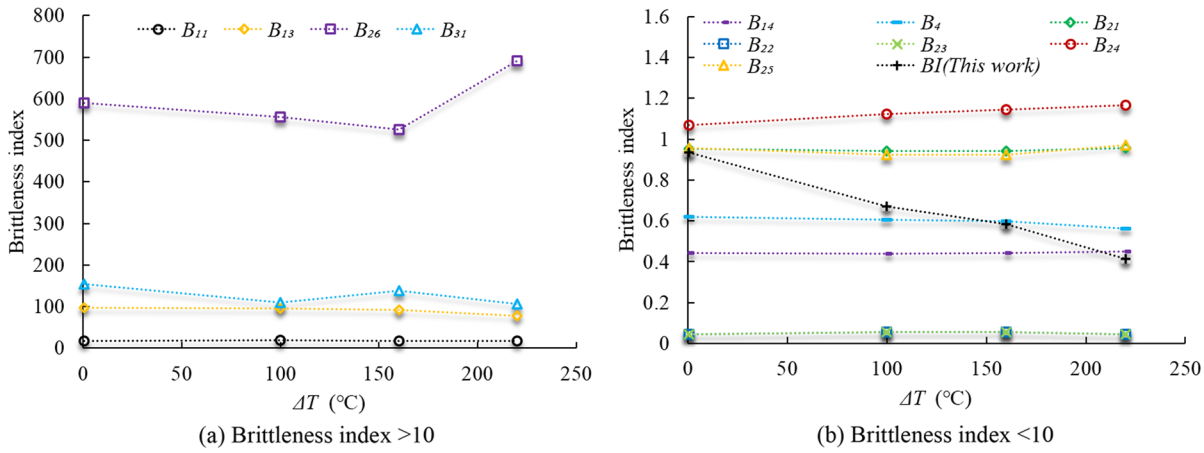

(a) Brittleness index >10 (b) Brittleness index <10

Fig. 23 Comparison of results of different brittleness indices

Surprisingly, there is several orders of magnitude difference between the value of brittleness index when adopting different methods. Compared with B_{22} having the minimum index value, B_{12} index is greater by five orders of magnitude. For convenience, we divided these results into two categories with the brittleness index 10 as watershed to illustrate and compare their performance and plotted them separately in Fig. 23. As we can see, the brittleness evaluation indexes of B_{13}, B_4, B_{23}, and BI decrease with the increase of temperature increment, which is consistent with the above analysis. Based on the expression of brittleness index B_{13} in Table 4, it can be seen that the value of B_{13} is associated with the crack initiation stress σ_{ci}. However, the acquisition of σ_{ci} is greatly affected by artificial factors when selecting the inflection point of the sample crack volume, therefore the value of B_{13} is essentially influenced by subjective judgement. Although the brittleness index of B_4 shows a declined trend with increased temperature, it is not sensitive to the influence of temperature with a narrow variation range. As for the brittleness index of B_{23}, it can only reflect the characteristics of the pre-peak stress–strain curve of the rock while ignoring post-peak characteristics.

On the other hand, B_{11}, B_{14}, B_{21}, B_{22}, B_{25}, B_{26}, and B_{31} fluctuate with increasing temperature, indicating that these brittleness indices are not very sensitive to changes in temperature, thus fail to reflect the influence of temperature on the brittleness of granite. It's worth noting that B_{24} shows an increasing trend with the increase in temperature, which is completely opposite to the analysis results, thereby cannot capture the negative relationship between the brittleness index and temperature. In summary, the brittleness index BI proposed in this paper can avoid the above problems and has a better performance in the brittleness evaluation of Gonghe granite. It can not only accurately describe the relationship between brittleness and temperature but also capture the strong dependent trend well.

5 Conclusions

The conclusions are summarized as follows:

(1) Generally, the peak strength demonstrates a monotonically decrease trend with the increase in temperature. The peak stress is decreased by 30.72% and the σ_{ci} and σ_{cd} are reduced by 24.17% and 39.37%, respectively when the temperature rises from RT to 240 °C. Through the normalization study, it is found that the influence of temperature on these parameters presents two distinct phases, and the critical temperature is around 180℃.

(2) Based on the multi-scale observations (e.g., 3D laser scanning, ultra-depth-of-field 3D optical microscope, and SEM), the roughness of micro and mesostructure of the fracture surface depends on the temperature conditions. The higher temperature would lead to the smooth surface structure.

(3) The *JRC* value, calculated from the results obtained by 3D laser scanning, decreases rapidly as temperature increases, indicating that the increase in temperature significantly reduces the roughness of the fracture surface. Meanwhile, the brittleness strength demonstrates the analogous behaviors as temperature changes, which is positively related to rock roughness.
(4) Combing with the pre-peak energy index and post-peak fracture *JRC*, a novel brittleness index calculation method of rock is developled, which can well capture the brittleness characteristics of high-brittle granites and avoid the difficulties in obtaining post-peak parameters, demonstrating superior performances compared with conventional models.

Author contribution ZL: Conceptualization, Methodology, Writing original draft, Revising, Validation, Funding acquisition; CW: Conceptualization, Writing original draft, Editing; MZ: Formula Analysis and Editing; JS: Discussion.

Funding This work was partially supported by the National Natural Science of Foundation of China (no. 52278333), and the Science and Technology Program of Tibet Province (no. XZ202101ZD0001G). The work is also supported by the 111 Project (B17009) and under the framework of the Sino-Franco Joint Research Laboratory on Multiphysics and Multiscale Rock Mechanics.

Data availability Any data and code used in this study can be available by requesting the corresponding author by email.

Declarations

Ethical approval The authors confirm their Ethics Approval.

Consent to publish The authors confirm their consent to publish.

Competing interests The authors declare no conflict of interest in this paper.

References

Altindag R (2002) The evaluation of rock brittleness concept on rotary blast hold drills. J South Afr Inst Min Metall 102(1):61–66

Aubertin M, Gill DE, Simon R (1994) On the use of the brittleness index modified (BIM) to estimate the post-peak behavior of rocks. 1st North American rock mechanics symposium OnePetro

Barton N, Choubey V (1977) The shear strength of rock joints in theory and practice. Rock Mech 10(1):1–54

Belem T, Homand Etienne F, Souley M (2000) Quantitative parameters for rock joint surface roughness. Rock Mech Rock Eng 33(4):217–242

Bishop A (1967) Progressive failure-with special reference to the mechanism causing it. Proc Geotech Conf, Oslo, pp 142–150

Brotons V, Tomás R, Ivorra S, Alarcón JC (2013) Temperature influence on the physical and mechanical properties of a porous rock: San Julian's calcarenite. Eng Geol 167:117–127

Chen YL, Ni J, Shao W, Azzam R (2012) Experimental study on the influence of temperature on the mechanical properties of granite under uni-axial compression and fatigue loading. Int J Rock Mech Min Sci 56:62–66

Fang XY, Xu JY, Liu S, Wang P (2016) Research on splitting-tensile tests and thermal damage of granite under post-high temperature. Chin J Rock Mech Eng 35(S1):2687–2694

Fardin N (2008) Influence of structural non-stationarity of surface roughness on morphological characterization and mechanical deformation of rock joints. Rock Mech Rock Eng 41(2):267–297

Feng XT, Haimson B, Li XC, Chang CD (2019) ISRM suggested method: determining deformation and failure characteristics of rocks subjected to true triaxial compression. Rock Mech Rock Eng 52(6):2011–2020

Feng Z, Zhao Y, Zhang Y, Wan Z (2018) Real-time permeability evolution of thermally cracked granite at triaxial stresses. Appl Ther Eng 25(133):194–200

Gao Y, Feng X, Zhang X, Feng G, Jiang Q, Qiu S (2018) Characteristic stress levels and brittle fracturing of hard rocks subjected to true triaxial compression with low minimum principal stress. Rock Mech Rock Eng 51(12):3681–3697

Gao Z, Liu Z, Tian F, Shen W (2022) Strength, energy evolution and cracking process of sandstone under high-temperature and high-pressure coupled true triaxial compression. Geomech Geophys Geo-Energy Geo-Resour 8(6):1–19. https://doi.org/10.1007/s40948-022-00490-3

Gong F, Yan J, Li X, Luo S (2019) A peak-strength strain energy storage index for rock burst proneness of rock materials. Int J Rock Mech Min Sci 1(117):76–89

Guo LL, Zhang YB, Zhang YJ, Yu ZW, Zhang JN (2018) Experimental investigation of granite properties under different temperatures and pressures and numerical analysis of damage effect in enhanced geothermal system. Renew Energy 126:107–125

Heinze T, Frank S, Wohnlich S (2021) FSAT–A fracture surface analysis toolbox in MATLAB to compare 2D and 3D surface measures. Comput Geotech 132:103997

Huang XX, Zhu JL, Li J, Bai B, Zhang GW (2016) Fluid friction and heat transfer through a single rough fracture in granitic rock under confining pressure. Int Commun Heat Mass Transf 75:78–85

Hucka V, Das B (1974) Brittleness determination of rocks by different methods. Int J Rock Mech Min Sci Geomech Abstr 11(10):389–392

Kahraman S, Altindag R (2004) A brittleness index to estimate fracture toughness. Int J Rock Mech Min Sci 41(2):343–348

Kidybiński A (1981) Bursting liability indices of coal. Int J Rock Mech Min Sci Geomech 18:295–304

Kivi IR, Ameri M, Molladavoodi H (2018) Shale brittleness evaluation based on energy balance analysis of stress-strain curves. J Petrol Sci Eng 167:1–19

Kuang Z, Qiu S, Li S, Du S, Huang Y, Chen X (2021) A new rock brittleness index based on the characteristics of complete stress–strain behaviors. Rock Mech Rock Eng 54:1109–1128

Kumari WGP, Ranjith PG, Perera MSA, Shao S, Chen BK, Lashin A et al (2017) Mechanical behaviour of Australian Strathbogie granite under in-situ stress and temperature conditions: an application to geothermal energy extraction. Geothermics 65:44–59. https://doi.org/10.1016/j.geothermics.2016.07.002

Lei Z, Zhang Y, Yu Z, Hu Z, Li L, Zhang S et al (2019) Exploratory research into the enhanced geothermal system power generation project: the Qiabuqia geothermal field. Northwest China Renew Energy 139:52–70

Li ZW, Feng XT, Zhang YJ, Gong YH, Zhu GQ (2020) Effect of mechanical damage on the thermal conductivity of granite. Rock Mech Rock Eng 53(3):1039–1051

Li B, Ju F, Xiao M, Ning P (2019) Mechanical stability of granite as thermal energy storage material: an experimental investigation. Eng Fract Mech 211:61–69

Li ZW, Long MC, Feng XT, Zhang YJ (2021) Thermal damage effect on the thermal conductivity inhomogeneity of granite. Int J Rock Mech Min Sci 138:104583

Liu Z, Wang H, Li Y, Wang X, Selvadurai APS (2022) Triaxial compressive strength, failure, and rockburst potential of granite under high-stress and ground-temperature coupled conditions. Rock Mech Rock Eng. https://doi.org/10.1007/s00603-022-03066-5

Liu S, Xu JY (2015) An experimental study on the physico-mechanical properties of two post-high-temperature rocks. Eng Geol 185:63–70

Liu J, Zhang LM, Cong Y, Wang ZQ (2021) Research on the mechanical characteristics of granite failure process under true triaxial stress path. Rock Soil Mech 42(8):2069–2077

Lu SM (2018) A global review of enhanced geothermal system (EGS). Renew Sustain Energy Rev 81:2902–2921

Luan Xy, Di Br, Wei Jx, Li Xy, Qian K, Xie Jy, et al (2014) Laboratory measurements of brittleness anisotropy in synthetic shale with different cementation. 2014 SEG annual meeting: onepetro

Ma X, Wang GL, Hu DW, Liu YG, Zhou H, Liu F (2020) Mechanical properties of granite under real-time high temperature and three-dimensional stress. Int J Rock Mech Min Sci 136:104521

Mahmutoglu Y (1998) Mechanical behaviour of cyclically heated fine grained rock. Rock Mech Rock Eng 31(3):169–179

Martin CD (1996) Brittle failure of rock materials: test results and constitutive models. Can Geotech J 33(2):378

Masri M, Sibai M, Shao JF, Mainguy M (2014) Experimental investigation of the effect of temperature on the mechanical behavior of Tournemire shale. Int J Rock Mech Min Sci 70:185–191

Mb G, Tf Li, Gq C, Lb M, Cc Li, Zhang Y et al (2022) Brittleness evaluation method based on pre-peak crack initiation and post-peak characteristics of rock. Chin J Geotech Eng 44(4):762–768

Meng F, Wong LNY, Zhou H (2021) Rock brittleness indices and their applications to different fields of rock engineering: a review. J Rock Mech Geotech Eng 13(1):221–247

Meng F, Zhou H, Zhang C, Xu R, Lu J (2015) Evaluation methodology of brittleness of rock based on post-peak stress–strain curves. Rock Mech Rock Eng 48:1787–1805

Miao ST, Pan PZ, Yu PY, Zhao SK, Shao CY (2020) Fracture analysis of Beishan granite after high-temperature treatment using digital image correlation. Eng Fract Mech 225:106847

Munoz H, Taheri A, Chanda E (2016a) Fracture energy-based brittleness index development and brittleness quantification by pre-peak strength parameters in rock uniaxial compression. Rock Mech Rock Eng 49(12):4587–4606

Munoz H, Taheri A, Chanda E (2016b) Rock drilling performance evaluation by an energy dissipation based rock brittleness index. Rock Mech Rock Eng 49(8):3343–3355

Nejati HR, Ghazvinian A (2014) Brittleness effect on rock fatigue damage evolution. Rock Mech Rock Eng 47(5):1839–1848

Nejati H, Moosavi SA (2017) A new brittleness index for estimation of rock fracture toughness. J Min Environ 8(1):83–91

Olasolo P, Juárez M, Morales M, Liarte I (2016) Enhanced geothermal systems (EGS): a review. Renew Sustain Energy Rev 56:133–144

Olgay Y, Eren S (2011) The effect of mechanical rock properties and brittleness on drillability. Sci Res Essays 6(5):1077–1088

Özfırat MK, Yenice H, Şimşir F, Yaralı O (2016) A new approach to rock brittleness and its usability at prediction of drillability. J Afr Earth Sc 119:94–101

Protodyakonov M (1962) Mechanical properties and drillability of rocks. Proceedings of the 5th symposium on rock

mechanics: University of Minnesota Minneapolis, Minnesota, USA p. 118
Rathnaweera T, Ranjith P, Gu X, Perera M, Kumari W, Wanniarachchi W et al (2018) Experimental investigation of thermomechanical behaviour of clay-rich sandstone at extreme temperatures followed by cooling treatments. Int J Rock Mech Min Sci 107:208–223
Shang X, Zhang Z, Xu X, Liu T, Xing Y (2019) Mineral composition, pore structure, and mechanical characteristics of pyroxene granite exposed to heat treatments. Minerals 9(9):553
Siratovich P, Heap M, Villeneuve M, Cole J, Kennedy B, Davidson J et al (2016) Mechanical behaviour of the Rotokawa Andesites (New Zealand): insight into permeability evolution and stress-induced behaviour in an actively utilised geothermal reservoir. Geothermics 64:163–179
Sun SZ, Wang KN, Yang P, Li XG, Sun JX, Liu BH, et al. (2013) Integrated prediction of shale oil reservoir using pre-stack algorithms for brittleness and fracture detection. International petroleum technology conference: OnePetro
Tarokh A, Peng J, Fakhimi A, Labuz JF (2016) Evaluation of brittleness from spalling and bending tests. 50th US rock mechanics/geomechanics symposium OnePetro
Tse R, Cruden D (1979) Estimating joint roughness coefficients. Int J Rock Mech Min Sci Geomech Abstr 5:303–307
Wang CP, Chen L, Liu JF, Liu J (2015) Experimental characterisation of thermo-mechanical coupling properties of Beishan granite. Eur J Environ Civ Eng 19(1):29–42
Wang K, Liu Z, Zeng T, Wang F, Shen W, Shao J (2022) Performance of enhanced geothermal system with varying injection-production parameters and reservoir properties. Appl Therm Eng 207:118160. https://doi.org/10.1016/j.applthermaleng.2022.118160
Wang C, Liu Z, Zhou H, Wang K, Shen W (2022) A novel true triaxial test device with a high-temperature module for thermal-mechanical property characterization of hard rocks. Eur J Environ Civ Eng. https://doi.org/10.1080/19648189.2022.2092214
Wang S, Zhao W, Fu X, Zhang Z, Wang T, Ge J (2020) A universal method for quantitatively evaluating rock brittle-ductile transition behaviors. J Pet Sci Eng 1(195):107774
Wong LNY, Zhang YH, Wu ZJ (2020) Rock strengthening or weakening upon heating in the mild temperature range? Eng Geol 272:105619
Wu XG, Huang ZW, Song HY, Zhang SK, Cheng Z, Li R et al (2019) Variations of physical and mechanical properties of heated granite after rapid cooling with liquid nitrogen. Rock Mech Rock Eng 52(7):2123–2139
Xu X, Karakus M (2018) A coupled thermo-mechanical damage model for granite. Int J Rock Mech Min Sci 103:195–204
Yagiz S (2009) Assessment of brittleness using rock strength and density with punch penetration test. Tunn Undergr Space Technol 24(1):66–74
Yan CZ, Zheng H (2017) A coupled thermo-mechanical model based on the combined finite-discrete element method for simulating thermal cracking of rock. Int J Rock Mech Min Sci 91:170–178
Yang SQ, Huang YH, Tian WL (2021) Influence of water saturation and real-time testing temperature on mechanical behavior of sandstone under conventional triaxial compression. Rock Mech Rock Eng 54(8):4355–4367
Yarali O, Kahraman S (2011) The drillability assessment of rocks using the different brittleness values. Tunn Undergr Space Technol 26(2):406–414
Yin WT, Feng ZJ, Zhao YS (2021) Effect of grain size on the mechanical behaviour of granite under high temperature and triaxial stresses. Rock Mech Rock Eng 54(2):745–758
Yong R, Ye J, Liang QF, Huang M, Du SG (2018) Estimation of the joint roughness coefficient (JRC) of rock joints by vector similarity measures. Bull Eng Geol Env 77(2):735–749
Zhang ZZ, Gao F, Liu ZJ (2010) Research on rockburst proneness and its microcosmic mechanism of granite considering temperature effect. Chin J Rock Mech Eng 29(8):1591–1602
Zhang L, Jiang PX, Wang ZC, Xu RN (2017) Convective heat transfer of supercritical CO_2 in a rock fracture for enhanced geothermal systems. Appl Therm Eng 115:923–936
Zhang P, Mishra B, Heasley KA (2015) Experimental investigation on the influence of high pressure and high temperature on the mechanical properties of deep reservoir rocks. Rock Mech Rock Eng 48(6):2197–2211
Zhang D, Ranjith PG, Perera MS (2016) The brittleness indices used in rock mechanics and their application in shale hydraulic fracturing: a review. J Pet Sci Eng 1(143):158–170
Zhang FZ, Xu RN, Jiang PX (2016) Thermodynamic analysis of enhanced geothermal systems using impure CO_2 as the geofluid. Appl Therm Eng 99:1277–1285
Zhang X, Xu J, Shaikh F, Sun L, Cao Y (2022) Rock brittleness evaluation index based on ultimate elastic strain energy. Processes 10(7):1367
Zhang F, Zhao JJ, Hu DW, Skoczylas F, Shao JF (2018) Laboratory investigation on physical and mechanical properties of granite after heating and water-cooling treatment. Rock Mech Rock Eng 51(3):677–694
Zhao J, Tang CA, Wang SJ (2020) Excavation based enhanced geothermal system (EGS-E): introduction to a new concept. Geomech Geophys Geo-Energy Geo-Resour 6(1):1–7
Zhao YS, Wan ZJ, Feng ZJ, Xu ZH, Liang WG (2017) Evolution of mechanical properties of granite at high temperature and high pressure. Geomech Geophys Geo-Energy Geo-Resour 3(2):199–210
Zhao YS, Wan ZJ, Feng ZJ, Yang D, Zhang Y, Qu F (2012) Triaxial compression system for rock testing under high temperature and high pressure. Int J Rock Mech Min Sci 52:132–138
Zhao XG, Xu HR, Zhao Z, Guo Z, Cai M, Wang J (2019) Thermal conductivity of thermally damaged Beishan granite under uniaxial compression. Int J Rock Mech Min Sci 115:121–136

Zhao XG, Zhao Z, Guo Z, Cai M, Li X, Li PF et al (2018) Influence of thermal treatment on the thermal conductivity of Beishan granite. Rock Mech Rock Eng 51(7):2055–2074

Zhou H, Liu Z, Shen W, Feng T, Zhang G (2022) Mechanical property and thermal degradation mechanism of granite in thermal-mechanical coupled triaxial compression. Int J Rock Mech Min Sci 1(160):105270

Zhou HW, Wang ZH, Ren WG, Liu ZL, Liu JF (2019) Acoustic emission based mechanical behaviors of Beishan granite under conventional triaxial compression and hydro-mechanical coupling tests. Int J Rock Mech Min Sci 123:104125